scientific reports

OPEN

Complex immune network and regional consistency in the human gastric mucosa revealed by high-resolution spectral cytometry

Ángel De Prado[1,7], Paloma Cal-Sabater[1,7], Aida Fiz-López[1], Sandra Izquierdo[2], Daniel Corrales[3], Francisco Pérez-Cózar[4], Juan H-Vázquez[1], Elisa Arribas-Rodríguez[1], Cándido Perez-Segurado[1], Álvaro Martín Muñoz[5], José A. Garrote[1], Eduardo Arranz[1], Concepción Marañón[4], Sara Cuesta-Sancho[1,8], Luis Fernández-Salazar[2,8] & David Bernardo[1,6,8✉]

The immune cellular landscape from the gastric mucosa remains largely unknown despite its relevance in several inflammatory conditions. Human gastric biopsies were obtained from the antrum, body and incisura from 10 individuals to obtain lamina propria mononuclear cells that were further characterized by spectral cytometry. Phenotypic hierarchical analyses identified a total of 52 different immune cell subsets within the human gastric mucosa revealing that T-cells (> 60%) and NK cells (> 20%) were the main populations. Within T-cells, CD4^{+} and CD8^{+} were equally represented with both subsets displaying mainly a memory and effector phenotype. NK cells, on the contrary, were largely of the early phenotype. No regional differences were observed for any subsets among the 3 locations. Following unsupervised analysis, a total of 82 clusters were found. Again, no differences were observed amongst locations although a great degree of inter-individual variability was found, largely influenced by the presence of *H. pylori* infection and dyspepsia. We have unraveled the human gastric immune cellular subset composition and a unique interindividual immune fingerprint with no inter-regional variations.

Keywords Spectral cytometry, Stomach, Human, Immunome, Gastric, *H. pylori*

The recent implementation of top-of-the-art mass cytometry (CyTOF) and spectral cytometry, have revolutionized the study of the human intestinal immune system, as these techniques provide a pseudo-omic resolution level[1–5]. Hence, these approaches provide the basis to perform an unbiased characterization of the human immune system (or immunome) found in the human intestinal mucosa in the context of several pathologies including malignancies, like colorectal cancer[6,7], but also autoimmune diseases like coeliac disease[8] and inflammatory bowel disease[9–11]. However, and as opposed to the duodenum, ileum or human colon, the composition of the human gastric mucosa immune system remains largely unknown despite its relevance in several immune mediated conditions like gastritis, *Helicobacter pylori* infection or gastric cancer.

Therefore, there is a real need to characterize and understand the human gastric immune system. The normal gastric mucosa is divided into two compartments and includes the gastrin and mucus-secreting glands of the antrum, and the acid and pepsinogen-secreting oxyntic glands of the corpus. Chronic gastritis progresses to atrophic gastritis and intestinal metaplasia, which increases the risk of gastric dysplasia and adenocarcinoma. These changes extend from gastric antrum to corpus, as Correa described[12], so the Sydney protocol taking biopsies from antrum, incisura and body is recommended for an early detection of premalignant conditions[13].

[1]Mucosal Immunology Lab, Unit of Excellence, Institute of Biomedicine and Molecular Genetics (IBGM), University of Valladolid-CSIC, Sanz y Forés 3., 47003 Valladolid, Spain. [2]Gastroenterology Department, Hospital Clínico, Universitario (HCUV-SACYL), University of Valladolid, Valladolid, Spain. [3]Pathology Department, Hospital Clínico, Universitario (HCUV-SACYL). Valladolid, Valladolid, Spain. [4]Pfizer-University of Granada-Junta de Andalucía Centre for Genomics and Oncological Research (GENYO), PTS, Granada, Spain. [5]Flow Cytometry Facility. Unit of Excellence Instituto de Biología y Genética Molecular (IBGM), University of Valladolid-CSIC, Valladolid, Spain. [6]Centro de Investigaciones Biomédicas en Red de Enfermedades Infecciosas (CIBERINFEC), Madrid, Spain. [7]These authors contributed equally: Ángel De Prado and Paloma Cal-Sabater. [8]These authors jointly supervised this work: Sara Cuesta-Sancho, Luis Fernández-Salazar and David Bernardo. ✉email: d.bernardo.ordiz@gmail.com

These glandular and mucosal changes could be associated with some immunological differences. Nevertheless, the properties of the immune system systematically change through the length of the gastrointestinal tract[14,15], something which can be found even within the same organ[16]. As a consequence, it is not just that the human gastric immune system is unknown, but also the presence of potential regional differences within these different anatomical locations.

In this regard, understanding the unique immune-related tissue structure of the gastric mucosa and its role in the immune response can help to prevent gastric diseases or treat them by immunotherapy, including not just *H. pylori* infection but also malignant processes. To that end, we have applied a spectral cytometry panel based on the OMIP-069[17], that we have already implemented in our lab[18,19] and which provides an in-depth immunophenotyping of all the major immune cell subsets, to characterize the immune infiltrate in the antrum, body and incisura of the human gastric mucosa. Our results provide, for the first time to our knowledge, a comprehensive unbiased characterization of the human gastric immunome, unravelling a complex leukocyte network. Indeed, we hereby also describe a single unique immune fingerprint and a lack of regional variation within the human gastric mucosa hence providing further input to study the local immune system in the context of several gastric pathologies.

Material and methods
Biological samples
A total of 10 controls (5 males, 5 females) with a median age of 62,5 years [interquartile range (IQR) 45–72 years] were recruited at the endoscopy unit of Hospital Clínico Universitario from Valladolid. Clinical and socio-demographic variables were also collected: gender, age, reason for endoscopy, treatment with NSAID, corticosteroids or proton pump inhibitors (PPI), presence and treatment of *H. pylori*, and histological findings are shown in Supplementary Table 1.

From each individual, a total of 4 biopsies were obtained from the prepyloric antrum, the incisura angularis and the body (lesser curvature). All samples were obtained by the same trained gastroenterologist (LFS). Two of them were used by the pathology department while the remaining two from each location were collected in ice-chilled complete medium [RPMI 1640 (Sigma-Aldrich, Dorset, UK) without L-glutamine (Gibco) and 10% foetal calf serum (TCS cellworks, Buckingham, UK)] and processed in the laboratory within 30 min.

All methods were carried out in accordance with relevant guidelines and regulations. All experimental protocols were approved by a named institutional and/or licensing committee (Committee from Valladolid Este -PI_22_2661-). Informed consent was obtained from all subjects and/or their legal guardian(s).

Sample processing
Mucosal biopsies were immediately processed as previously described[16,20] to obtain lamina propria mononuclear cells (LPMC) following two incubations (30 min each) with Hanks balanced salt solution (HBSS) (Gibco BRL, Paisley, Scotland, UK) containing 1 mM DTT and 1 mM EDTA solutions to remove the associated mucus/bacteria and epithelial layer, respectively, and subsequently digested by three incubations of 30 min each in presence of 1 mg/mL Collagenase D (Roche Diagnostics GmbH, Mannheim, Germany), 20 µg/mL Liberase (Roche Diagnostics GmbH, Mannheim, Germany), and Benzonase (25U/mL) (ThermoFisher Scientific, Bonn Germany). Cells were filtered through a 100-µm cell strainer and were collected by centrifugation to obtain LPMCs for further staining.

Antibody staining and cell acquisition
After isolation, LPMCs were stained with 38 monoclonal antibodies (Supplementary Table 2) to be characterised by spectral cytometry (CyTek Aurora 5-laser) following the guidelines displayed in the OMIP-069 protocol[17]. Briefly, before staining, Live/Dead fixable blue dead cell stain kit (Molecular Probes, Thermo Fisher Scientific) was added to the LPMC exclude dead cells from the analysis. Brilliant Stain Buffer and True-Stain Monocyte Blocker were also added prior to staining with the antibodies to obtain optimal fluorescence of the desired cells. LPMCs were further washed with FACS buffer (500 mL PBS + 10 mL filtered FCS + 0.1 g NaN_3 + 2.5 mL sterile EDTA) and incubated in the dark at room temperature during the staining process. Finally, cells were fixed with 0.8% paraformaldehyde in FACS buffer in the dark for 10 min and washed with FACS buffer to store at 4 °C, before being acquired on a 5-laser and 67-detector spectral cytometer (Aurora, Cytek) within 24 h.

Classical flow cytometry analysis
Results were analyzed following classical hierarchical gating strategies using FlowJo. In all cases, cells were analyzed within singlet viable cells. From there, different gating strategies were followed to identify the main cell populations of the immune system (granulocytes, basophils, macrophages, dendritic cells, NK cells, innate lymphoid cells, B-cells, and T-cells) as well as other subsets as detailed in Fig. 1A. Given the large number of identified T-cells, they were further identified in depth as displayed in Fig. 1B. In total, we could hierarchically identify 52 different subsets, for which their relative proportion within single viable leukocytes was determined. All gates were set up using the fluorescence minus one (FMO) approach. In addition, and within each identified immune cell subset, the expression levels of NKG2a, NKG2c, NKG2d, NKP30, CCR5, CCR6, CXCR3, CXCR5, FAS, PD-1 and CD57 was determined using the fluorescence intensity (MFI).

Computational cytometry analysis
Due to the large amount of data obtained with this panel, it is not advisable to examine data exclusively through traditional manual identification due to its subjectivity, but also because some immune subsets may go unnoticed. To that end, results were also analyzed using the OMIQ® software from Dotmatics (www.omiq.ai, www.dotmatics.com). Hence, the first step was to transform the data using the scale, parameters and cofactors
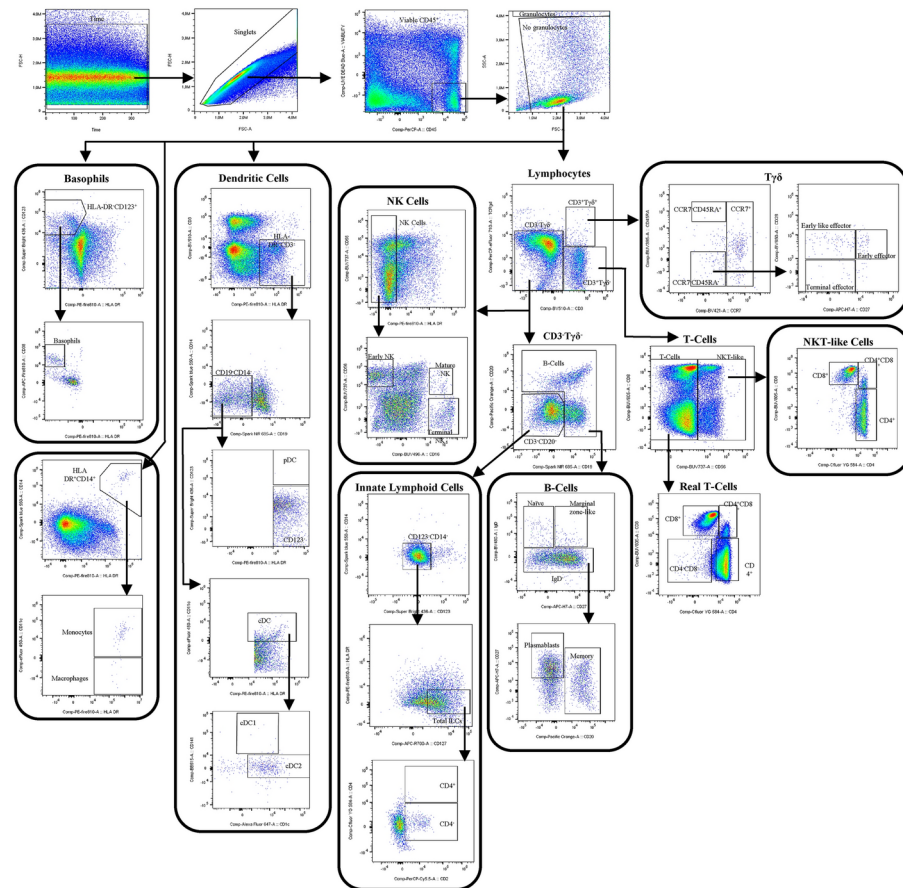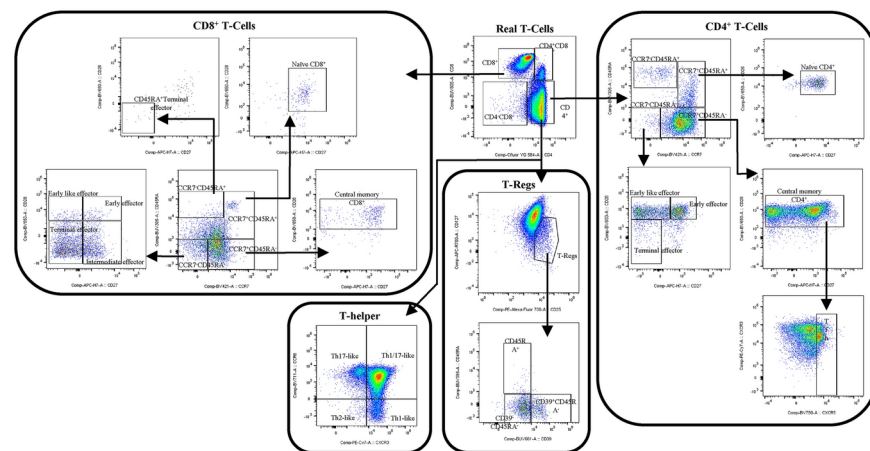
Fig. 1. Immune cell subset identification in the human gastrointestinal mucosa The gating strategy to identify the different immune (within singlet viable leucocytes) in the human gastric mucosa is shown in **A**. Given the large number of T-cell subsets that can be found, their specific gating strategy is shown in **B**.

suggested by the OMIQ software. Data cleaning algorithm FlowAI was applied in order to remove outlier events in spectral cytometry data files due to abnormal flow behaviors resulting from clogs and other common technical problems. Subsequently, a manual discard to eliminate cell debris and doublets and to select viable leukocytes (CD45$^+$ cells) was performed and cleaned data were used for subsequent analysis.

Following that, an unsupervised approach applying UMAP algorithm was used for the exploratory analysis. Briefly, this algorithm uses a non-linear method based on graphs constructed to represent information in multiple dimensions, and then reconstructs the results into a two-dimensional map, preserving the multidimensional structure. In this way, the algorithm finds similarities between cells in all dimensions. These dimensions are, in our case, the markers that they express and their levels of expression. The algorithm returns a two-dimensional map where the proximity of cells reflects their distances in multidimensional space, such that cells with similar patterns of expression were located very close. This distance/similarity relationship is respected within and between each group or islet. Due to the technical limitations of the software, a prior subsampling or random selection of events was performed until the total of 4 million events was reached, so each cohort was equally represented. To run the algorithm, phenotypic and functional markers were used in OMIQ Data Science platform with the following parameters: neighbors: 15, minimum distance: 0.4, metric: euclidean, number of components: 2, seed: 8287, learning_rate: 1, epochs: 200, embedding initialization: spectral.

Subsequently, the FlowSOM algorithm was applied to find similar cell populations and separate them into groups or "metaclusters" in an unsupervised manner. Briefly, this algorithm analyzes the expression of all the selected markers in each of the cells of each sample and then groups them into clusters according to their expression level. In this way, it not only allows for the visualization of cells in typical biological groupings, but also for the detection of new or unexpected populations. However, this algorithm only showed metaclusters that would represent the large populations of the immune system present in the sample. Parameters used for the algorithm were: phenotypic and functional markers (the same as for the UMAP algorithm), umap_1 and umap_2 (outputs from the UMAP algorithm), number of clusters: 100 (10 in the X dimension, 10 in dimension Y), number of training iterations: 10, distance metric: Euclidean, method: Elbow Metaclustering, Random Seed: 190. The visual representation merge of the two algorithms, allowed us to subdivide these metaclusters into clusters representing more accurately all the phenotypic and functional subsets presented in our samples.

Next, a clustered heatmap was created using the previously obtained clusters. This heatmap graphically represent the level of expression of each cluster, sample or group under study, of each of the phenotypic markers and, in turn, associate by similarity (distance) the clusters forming a dendrogram. This approach allows to identify the immune subsets represented by each cluster based on the expression levels of their markers. In this way, if a specific cluster is associated with a condition under study, its phenotype could be elucidated to identify it using classical supervised approaches where it would otherwise have gone undetected. Finally, the refine results of FlowSOM algorithm were mapped on the UMAP in order to observe their distribution.

Statistical analysis

For the unsupervised analysis, volcano plots were constructed by comparing differences in clusters between gastric locations. This type of graph uses the total events into each cluster and combines a measure of statistical significance from a statistical test (e.g., a p value from an ANOVA model) with the magnitude of the change, enabling quick visual identification of clusters that display large change, that are also statistically significant.

For the hierarchical ones, GraphPad Prism9 was used to compare the cellular composition of the three stomach locations. The percentages of the total viable leukocytes fraction (CD45$^+$) of those subsets were obtained, and then the statistical analysis using GraphPad Prism9 were performed. Quantitative variables were expressed as mean and standard deviation as followed a normal distribution, and parametric t-student test were used. A p-value under 0.05 were considered statistically significant.

Results

Description of leukocyte subset composition in the stomach

A total of 52 different human gastric mucosa immune cells were identified as displayed in the gating strategy (Fig. 1A, B). A first analysis determined the relative proportion of the main immune populations found in the 30 study samples (10 individuals; 3 locations per individual), as shown in Fig. 2A, revealing that T-cells (characterized by CD3$^+$) were the main immune population in the human stomach (60.22%), followed by NK cells (22.24%), B-cells (7%), granulocytes (6.63%), ILCs, (3.54%), antigen presenting cells (0.19%) and basophils (0.18%) (Fig. 2A). The relative abundance of these subsets was also determined in the different locations (antrum, incisura and body), revealing no major differences among the 3 studied compartments (Fig. 2B).

Immune subsets in the human stomach

Given that T-cells are the main cell population found in the human stomach, they were further characterized in depth as described in Fig. 1B. CD8$^+$ (CD3$^+$CD56$^-$CD8$^+$) and CD4$^+$ T-cells (CD3$^+$CD56$^-$CD4$^+$) were almost equally represented in the T-cell compartment (44.22% and 38.57% respectively) in the human stomach. A total of 3.79% of double negative T-cells (CD3$^+$CD56$^-$CD4$^-$CD8$^-$) and 1.52% double positive T-cells (CD3$^+$CD56$^-$CD4$^+$CD8$^+$) were also found within total T-cells (Fig. 3A).

To deeply characterize the major helper T-cells, the expression of CD45RA$^+$, CCR7$^+$, CD27$^+$ and CD28$^+$ were used to further classified them into subsets based on their phenotypes (Fig. 3B). Hence, central memory cells were the main subset (CD45RA$^-$CCR7$^+$CD28$^+$, 84.45%) and, within them, 4.34% were Tfh (CD45RA$^-$CCR7$^+$CD28$^+$CXCR5$^+$, data not shown). The next most represented subset was early effector (CD45RA$^-$CCR7$^-$CD28$^+$CD27$^+$, 5.68%) cells, followed by early like effector (CD45RA$^-$CCR7$^-$CD28$^+$CD27$^-$, 4.56%), naïve (CD45RA$^+$CCR7$^+$CD28$^+$CD27$^+$, 2.70%), CD45RA$^+$CCR7$^-$ cells (1.79%) and terminal effector (CD45RA$^-$CCR7$^-$CD28$^-$CD27$^-$, 0.82%).

Helper T-cells were also classified into lineages, commonly referred to as T-helper (Th) following the gating strategy displayed in Fig. 1B, revealing a majority of Th1/Th17-like (CD3$^+$CD4$^+$CCR6$^+$CXCR3$^+$, 68.15%), followed by Th17-like (CD3$^+$CD4$^+$CCR6$^+$CXCR3$^-$, 17.20%), Th1-like (CD3$^+$CD4$^+$CCR6$^-$CXCR3$^+$, 11.63%) and Th2-like (CD3$^+$CD4$^+$CCR6$^-$CXCR3$^-$, 3.03%) (Fig. 3C).
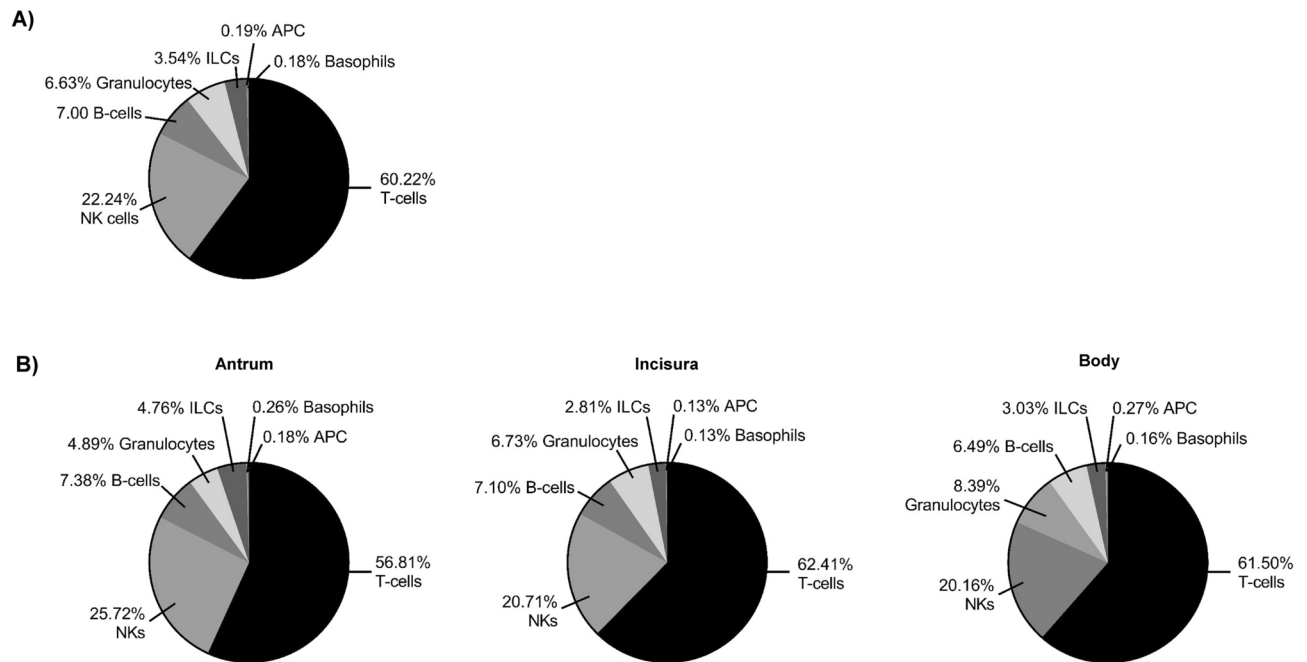
Fig. 2. Immune cell composition in the stomach (**A**) Cellular immune populations were identified as in Fig. 1 to display their general proportion in the human stomach as well as (**B**) within the antrum, incisura and body of the gastric mucosa.

In a similar manner, regulatory T-cells (T_{regs}) were identified as CD25$^+$CD127$^+$ and were further divided into CD39$^+$ T_{regs} (CD25$^+$CD127$^+$CD45RA$^-$CD39$^+$, 48.83%) and CD39$^-$ T_{regs} (CD25$^+$CD127$^+$CD45RA$^-$CD39$^-$, 47.32%). A small percentage (3.85%) of CD25$^+$CD127$^+$CD45RA$^+$ T_{regs} were also found (Fig. 3D).

Given that Tγδ-cells are particularly relevant in the gastrointestinal tract, they were also divided into effector/memory subsets. A majority of CD45RA$^+$CCR7$^+$ were found in the stomach (88.38%), followed by early like effector Tγδ cells (CD45RA$^-$CCR7$^-$ CD28$^+$CD27$^-$, 6.92%); CD45RA$^+$CCR7$^-$ (2.55%), terminal effector (CD45RA$^-$CCR7$^-$CD28$^-$CD27$^-$ 1.78%) and early effector (CD45RA$^-$CCR7$^-$CD28$^+$CD27$^+$, 0.37%) (Fig. 3E).

Finally, the relative proportion of the main cytotoxic subsets was also determined. Hence, CD8$^+$ T-cells were classified into central memory (CD45RA$^-$CCR7$^+$, 32.36%), CD45RA$^+$ terminal effector (CD45RA$^+$CCR7$^-$CD28$^-$CD27$^-$, 26.64%), terminal effector (CD45RA$^-$CCR7$^-$CD28$^-$CD27$^-$, 18.02%), intermediate effector (CD45RA$^-$CCR7$^-$CD28$^-$CD27$^+$, 12.57%), naïve (CD45RA$^+$CCR7$^+$CD28$^+$CD27$^+$, 4.55%), early effector (CD45RA$^-$CCR7$^-$CD28$^+$CD27$^+$, 3.63%) and early like effector (CD45RA$^-$CCR7$^-$CD28$^+$CD27$^-$, 2.23%) (Fig. 3F).

Having described the T-cell compartment, we next studied the proportion of the other immune cells. Hence, the analysis of NK cells revealed that the majority of them were early NKs (CD3$^-$HLADR$^-$CD16$^-$CD56$^+$, 61,91%) followed by mature NKs (CD3$^-$HLADR$^-$CD16$^+$CD56$^+$, 24.62%) and terminal NKs (CD3$^-$HLADR$^-$CD56$^-$CD16$^+$, 13.46%) (Fig. 3G).

In a similar manner, NKT cells were defined as CD3$^+$CD56$^+$, revealing most of them were CD8 (CD3$^+$CD56$^+$CD8$^+$, 67.28%) in the gastric mucosa, followed by CD4 (CD3$^+$CD56$^+$CD4$^+$, 28.62%) and finally double positive cells (CD3$^+$CD56$^+$CD4$^+$CD8$^+$, 4.11%) (Fig. 3G).

ILC were identified as CD3$^-$CD19$^-$CD20$^-$CD14$^-$CD123$^-$CD127$^+$CD2$^+$ and divided based on CD4 expression revealing a majority of CD4$^-$ ILCs (86.06%) referred to CD4$^+$ ILCs (13.94%) (Fig. 3G).

On the other hand, B-cells were defined as CD3$^-$Tγδ$^-$CD19$^+$CD20$^+$ and further subsetted into plasmablasts (CD3$^-$Tγδ$^-$CD19$^+$CD20$^-$CD27$^+$, 76.19%), memory B cells (CD3$^-$Tγδ$^-$CD19$^+$CD20$^+$, 17.59%), naïve B-cells (CD3$^-$Tγδ$^-$CD19$^+$CD20$^+$IgD$^+$CD27$^-$ 2.18%) and marginal zone-like B-cells (CD3$^-$Tγδ$^-$CD19$^+$CD20$^+$IgD$^+$CD27$^+$, 4.04%) (Fig. 3G).

Last, but not least, antigen presenting cells included type 2 conventional dendritic cells (CDC2; CD14$^-$CD19$^-$CD11c$^+$HLADR$^+$CD1c$^+$CD141$^-$, 60.92%), plasmacytoid dendritic cells (pDC; CD14$^-$CD19$^-$HLADR$^+$CD123$^+$, 35.44%) monocytes (CD14$^+$CD11c$^+$HLADR$^+$, 1.85%), macrophages (CD14$^+$CD11c$^-$HLADR$^+$, 1.18%) and finally type 1 conventional dendritic cells (cDC1; CD14$^-$CD19$^-$CD11c$^+$HLADR$^+$CD141$^+$ 0.62%) (Fig. 3G).

Unbiased characterization of the human gastric immune system

While the classical hierarchical gating provides relevant information regarding the known immune cell subsets compositions in a given sample, the use of complex panels, as in this case, can actually identify novel or specific subsets which otherwise would have been undetected. Hence, dimensionality reduction and clustering algorithms, like UMAP, provide powerful tools to preserve the local and global structure of the data. Figure 4A displays the general UMAP including the 30 analyzed samples (10 controls and, within each of them, 3 different
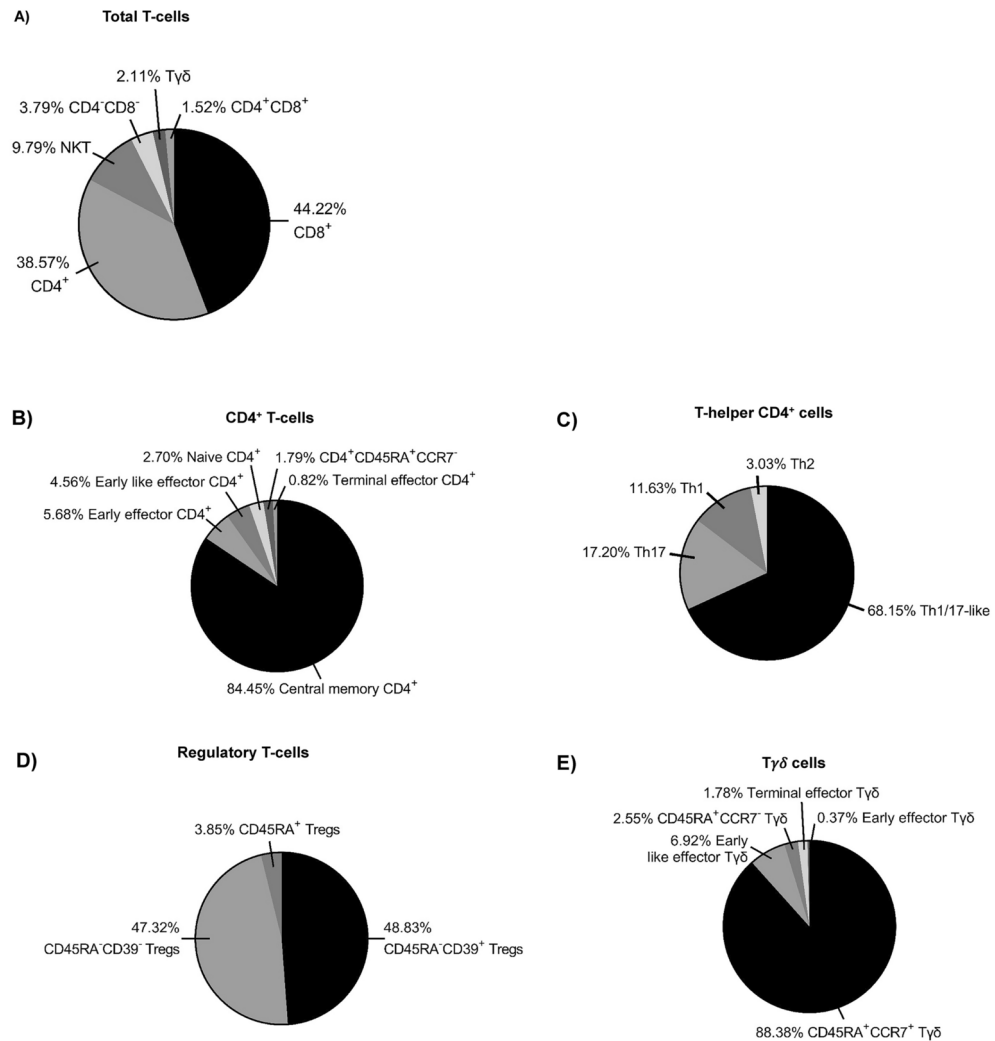
Fig. 3. Immune cell subsets in the human gut (**A**) Total T-cells were identified as in Fig. 1B to display their main subsets. Subsequent division into the different subsets of (**B**) effector, memory and naïve subsets within CD4⁺; (**C**) Th-type CD4⁺; (**D**) regulatory T-cells; (**E**) Tγδn and (**F**) CD8⁺ T-cells was perfomed. Non-T-cell immune cells are shown in (**G**).

locations -antrum, incisura and body-). The UMAP map identifies two major continents and a third pool of smaller islands derived from grouping phenotypically similar events. The relative expression of each marker on the UMAP is shown in Fig. 4B revealing that the main continent on the left represents cytotoxic T-cells, while the main continent on the right is made of helper T-cells. In a similar manner, the smaller islands on the north are mainly composed of B-cell and NK cells.

UMAP approach allowed us not only to identify the populations that were analyzed in a hierarchical way, but also to identify unexpected populations. Therefore, an unsupervised approach applying UMAP algorithm was used for the exploratory analysis. Subsequently, the FlowSOM algorithm was used to find similar cell subsets (clusters) and separate them into groups or "meclusters" in an unsupervised manner (Fig. 4C). That does not only allow the visualization of cells in typical biological groupings, but also for the detection of new or unexpected subsets. However, this algorithm only displayed metaclusters that would represent the large subsets of the immune cells present in the sample, in our case a total of 6 metaclusters were identified.

The visual representation of the two algorithms, UMAP and FlowSOM, allows to further subdivide these metaclusters into clusters representing more accurately all the phenotypic and functional subsets of the gastric immunome. A clustered heatmap was created using the clusters obtained in the previous point (Supplementary Fig. 1). This heatmap graphically represents the level of expression of each phenotypic marker, into each cluster. Dendrograms grouped clusters and phenotypic markers associated by similarity (distance). This approach permits to identify the immune subsets represented by each cluster based on the expression levels of their markers hence identifying a total of 82 clusters. Table 1 display the phenotype and identification of all the clusters, hence providing a deep phenotype identification for 81 of them, given that cluster 72 could not be identified. Besides, Table 1 reveals how different populations can be stratified into smaller subsets based on the expression of several surface markers. For instance, total terminal effector CD8⁺ T-cells, which can be identified in Fig. 1B,
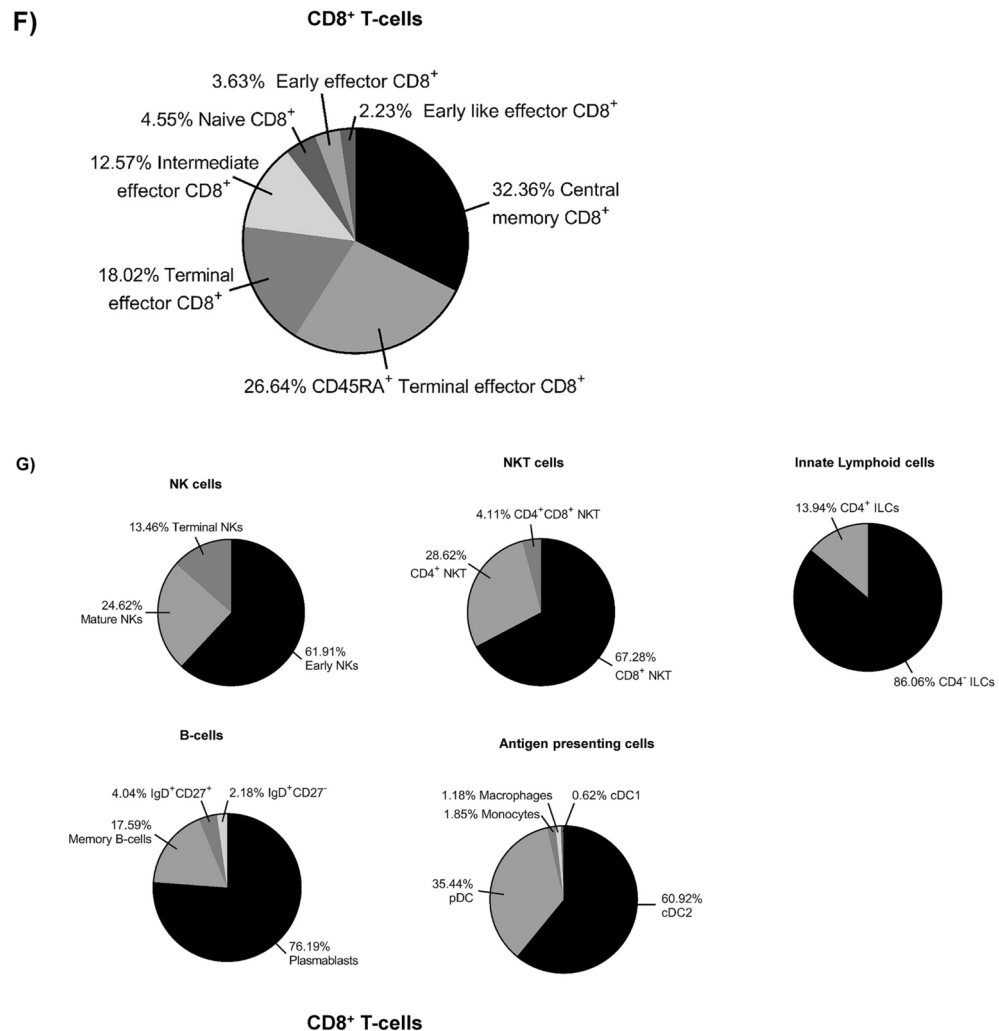
Figure 3. (continued)

can be nevertheless further divided into 19 different subsets based on the expression of several phenotypic and functional markers shown in Table 1. Hence, these analyses are therefore essential in order to further unravel the complex immune heterogenicity which can be found in a given sample.

Finally, these clusters were further uploaded into the UMAP (Fig. 4D) to determine how they relate one to each other.

Lack of regional immune variability within the human gastric mucosa

While classical hierarchical gating approaches suggest the lack of regional differences within the human gastric mucosa (Fig. 2B), these approaches had only identified a total of 52 classical subsets, while the unsupervised analyses have identified a total of 82 different clusters. Hence, further UMAP analysis was performed in the context of sample location (Fig. 5A). Although small differences between locations could be seen, only 1 out of the 82 clusters was differentially expressed among the antrum and the body (Fig. 5B) corresponding to cluster 72 in Table 1 of unknown origin.

The human gastric immunome displays a unique inter-individual immune fingerprint

Having described the lack of regional variability within the human gastric mucosa, we next addressed the degree of inter-individual variability. To that end, the relative contribution of each of the 10 recruited individuals was uploaded into the UMAP analysis revealing a unique immune fingerprint in the human gastric mucosa for each individual (Fig. 6A). Indeed, a volcano plot analysis comparing the relative proportion of the 82 clusters from the first individual referred to the other 9 controls revealed a huge degree of inter-individual variability (Fig. 6B).

In a similar manner, we also compared the effect that demographic variables could elicit on such variability, hence considering the effect of sex (Fig. 7A) and age (Fig. 7B), as well as of the presence of *H. pylori* infection (Fig. 7C), dyspepsia (Fig. 7D), or proton pump inhibitor consumption (Fig. 7E). In agreement with the great degree of inter-individual variability (Fig. 6), and as opposed to the mucosal location, they all impacted the mucosal cell composition since from the 82 different clusters, almost half of the clusters (38) were influenced
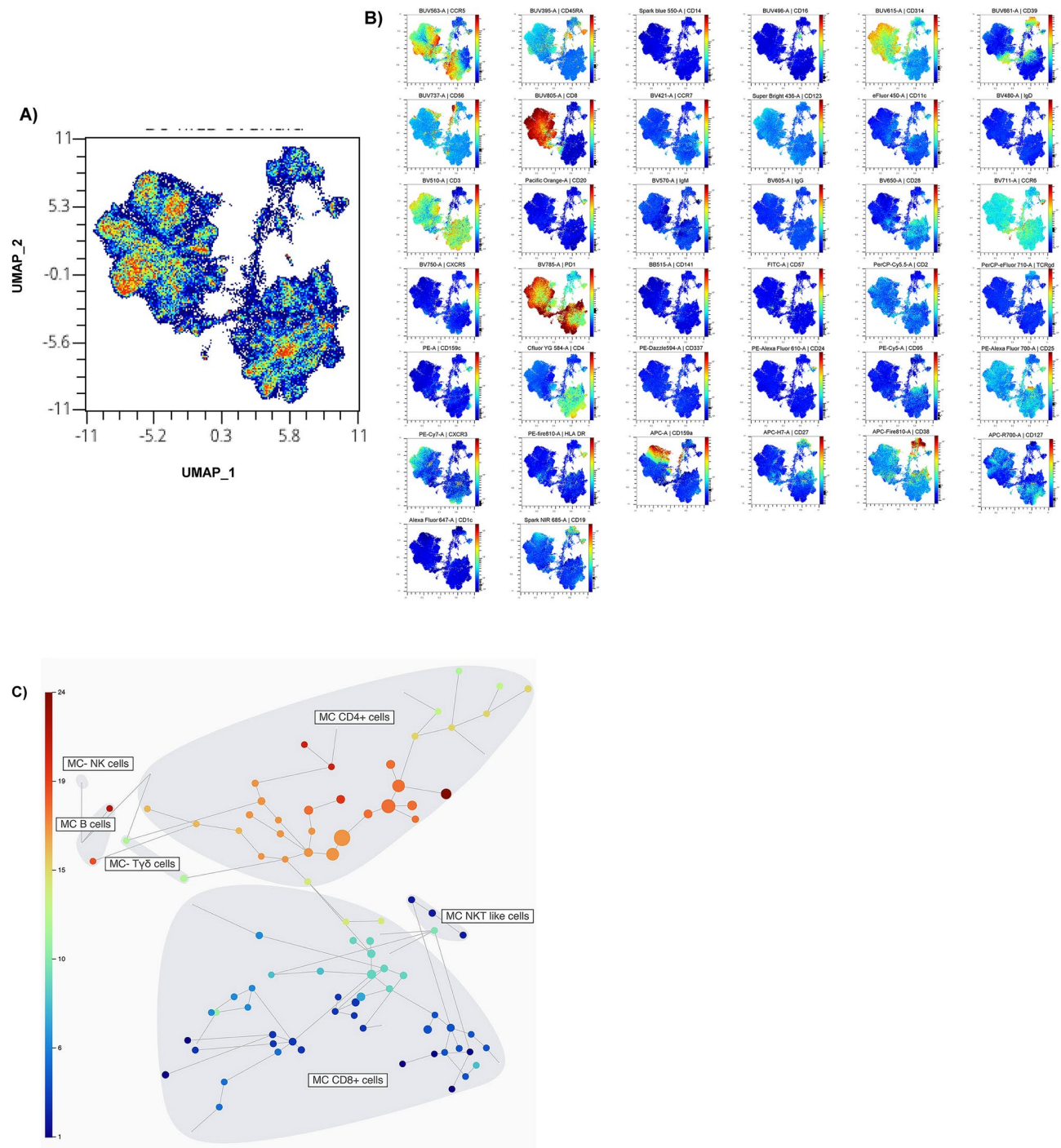
Fig. 4. Unbiased gastric immunome characterization (**A**) UMAP analysis within total singlet viable CD45+ cells from the human gastric mucosa from the antrum, body and incisura from ten individual was performed, showing in (**B**) the relative expression of each of the analyzed markers. (**C**) FlowSOM analysis was also performed to identify a total of 82 clusters. (**D**) The clusters were uploaded over the general UMAP in order to display the immune subsets and how they relate once to each other.

by these variables (Table 2). Further analyses revealed that both the age and the PPI consumption did not elicit a major effect on the immune variability as only 8 and 12 of the 82 clusters were significantly affected by them. On the contrary, 21 of the clusters were influenced by the sex (male/female), while the presence of *H. pylori* infection or dyspepsia had a major impact of the immune variability affecting the contribution of 31 and 32 clusters respectively. Besides, 22 of those clusters displayed the same trend on both variables hence confirming that correlation between *H. pylori* infection and dyspepsia, also affects the composition of the human gastric immune system.
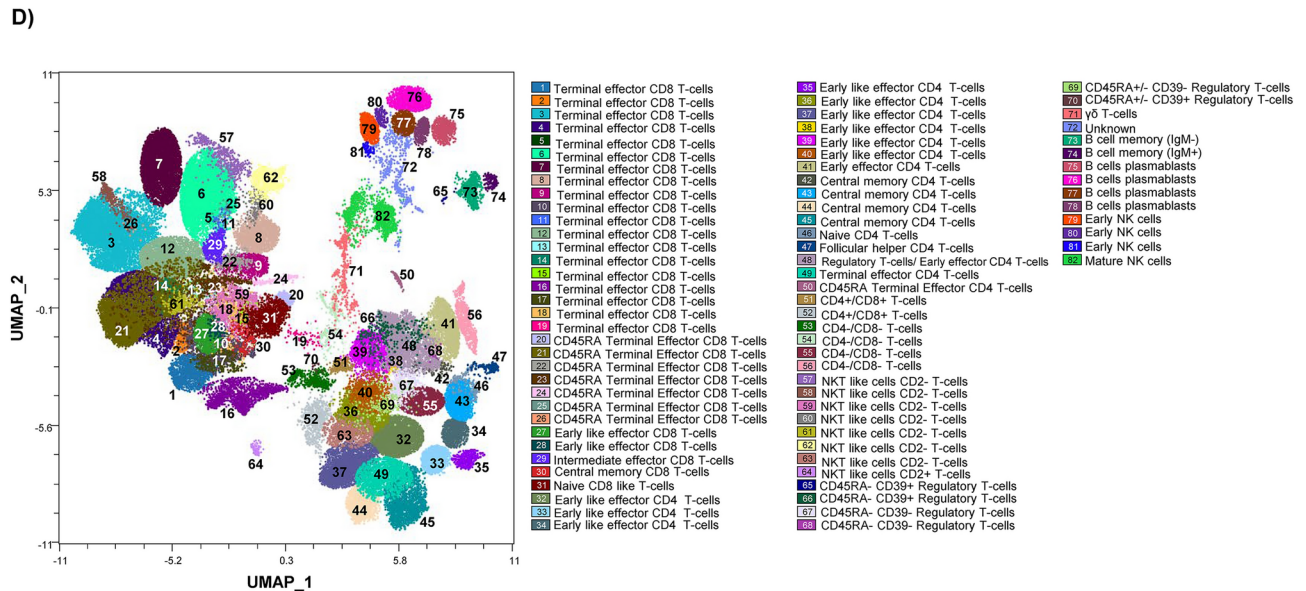
D)

Figure 4. (continued)

Discussion

We hereby have performed, for the first time to our knowledge, a comprehensive characterization of the fresh human gastric immunome describing how mucosal T-cells are the main immune cells in that compartment. Moreover, although the different anatomic parts of the stomach have clinical relevance as the risk of gastric cancer increases when intestinal metaplasia extends from the gastric antrum to the corpus, we have described that there are no immune regional differences among them. Furthermore, we have also shown how, despite the lack of inter-regional gastric immune variability, the human gastric mucosa displays a unique immune fingerprint confirming the presence of a great degree of inter-individual variability.

Gastric cancer mains one of the most commonly diagnosed cancer types in the world, also with a relatively high mortality rate, being *H. pylori* infection its main trigger[21]. Indeed, and in agreement with our observations, the composition of the human gastric immune system is impacted by *H. pylori* infection since it favors an increased recruitment of regulatory T-cells towards the gastric mucosa[22], mainly of a CD45RA-CD39+ phenotype (Table 2). Such increased recruitment of T_{reg} cell towards the gastric mucosa is mediated in a CCR4 and CCR6 dependent manner[23,24] hence providing a potential mechanism by which *H. pylori* infection can evade the host´s immune response. As a consequence, multiple studies are currently focusing on the characterization of the mucosal immune response not just following *H. pylori*, but also after gastric cancer onset and how that correlates with the clinical outcome. For instance, although microsatellite instability is associated with an increased in tumor-infiltrating lymphocytes (TIL), and a subsequent better prognosis, the same does not apply in patients with gastric cancer where, although microsatellite instability correlates with higher numbers of TIL, that however does not translate into a better prognosis[25]. In a similar manner, it has been described an increased expression of PD-L1 in gastric epithelial cells following in the course of *H. pylori* infection and subsequent progression towards gastric cancer[26]. Hence, not surprisingly, immune checkpoint inhibitor (ICI) therapy is gaining strength on the treatment of gastric cancer. However, only a small proportion of patients benefit from it. The reason underlaying this paradox remain obscure, but it seems to be related with tumor location since patients with gastric adenocarcinoma have a lower infiltrate of immune suppressive cell subsets coupled with increased levels of effector TIL referred to patients with a gastroesophageal one, hence explain why patients with gastric-specific adenocarcinoma (but not gastroesophageal) benefit more from ICI therapies[27]. Having therefore proved that the human gastric immune infiltrate can be unbiasedly characterized by spectral and computational cytometry, future studies can therefore follow this lead in order to comprehensively characterize the phenotype and function of TIL, and how that correlates with the clinical outcome of the patients.

One of the major findings of this study is that, , the immune system from the human gastric mucosa displays a great degree of interindividual variability coupled with a lack of regional variation as opposed to other compartments from the human intestine[15]. Given that the samples from each individual were individually processed in fresh, one may assume that such inter-individual variability could rely on a differential processing. Nevertheless, all biopsies were obtained by the same clinician and processed under the same conditions (including the same antibody cocktail). Besides, a differential depth of the biopsy sampling does not seem to be a reason underlying that since, that being the case, it might be expected that samples would randomly relate one to each other. On the contrary, a t-SNE analysis confirmed that samples grouped based on the donor irrespectively of the location (Fig. 8). Hence, the great degree of interindividual variability seems to be derived from the biological diversity among individuals. Besides, further analysis revealed how, despite the great degree of interindividual variability, the presence of *H. pylori* infection and dyspepsia has an impact on the composition of the human gastric cellular immunome (Table 2), including increased number of mucosal T_{regs}[22–24]. In this

Cluster	Population	Subset	Phenotipic expression	Functional expression
1	CD8+	Terminal effector (1)	CD3,CD8, **CD39**	CCR5, CXCR3, PD1, CD314/NKG2D
2	CD8+	Terminal effector (2)	CD3,CD8	CCR5, CXCR3, PD1, CD314/NKG2D, CD95/Fas, CD159c/NKG2C, HLA-DR
3	CD8+	Terminal effector (3)	CD3, CD8, **CD39**	CCR5, CXCR3, PD1, CD314/NKG2D, CD95/Fas
4	CD8+	Terminal Effector (4)	CD3, CD8	CCR5, CXCR3, PD1, CD314/NKG2D, CD95/Fas
5	CD8+	Terminal Effector (5)	CD3, CD8, **CD39dim**	CCR5, CXCR3, PD1, CD314/NKG2D, CD95/Fas, CD159a/NKG2A
6	CD8+	Terminal Effector (6)	CD3, CD8	CCR5, CXCR3, PD1, CD314/NKG2D, CD159a/NKG2A, CD95/Fas
7	CD8+	Terminal Effector (7)	CD3, CD8, **CD39**	CCR5, CXCR3, PD1, CD314//NKG2D, CD159a/NKG2A, CD95/Fas
8	CD8+	Terminal Effector (8)	CD3, CD8, **CD141, CD2dim**	CCR5, CXCR3, PD1, CD314/NKG2D,CD159a/NKG2A
9	CD8+	Terminal Effector (9)	CD3, CD8, **CD141**	CCR5, CXCR3, PD1, CD314/NKG2D, CD159c/NKG2C, CD95/Fas
10	CD8+	Terminal Effector (10)	CD3, CD8, **CD38dim, CD39**	CCR5, CD314/NKG2D, CD95/Fas
11	CD8+	Terminal Effector (11)	CD3, CD8, **CD38dim,**	CCR5, CXCR3, CD314/NKG2D, CD95/Fas, CD159a/NKG2A
12	CD8+	Terminal Effector (12)	CD3, CD8, **CD127dim**	CCR5, CXCR3, CD314/NKG2D
13	CD8+	Terminal Effector (13)	CD3, CD8	CCR5, CXCR3, CD314/NKG2D
14	CD8+	Terminal Effector (14)	CD3, CD8	CCR5, CXCR3, CD314/NKG2D, PD1
15	CD8+	Terminal Effector (15)	CD3, CD8	CCR5, CXCR3, CD314/NKG2D, CD95/Fas, CD159c/NKG2C
16	CD8+	Terminal Effector (16)	CD3, CD8, **CD39, CD2**	CCR5, PD1, CD95/Fas, CCR6
17	CD8+	Terminal Effector (17)	CD3, CD8, **CD39**	CCR5, PD1, CXCR3dim
18	CD8+	Terminal Effector (18)	CD3, CD8	CCR5
19	CD8+	Terminal Effector (19)	CD3, **CD8dim**	CCR5
20	CD8+	CD45RA Terminal Effector (1)	CD3, CD8, CD45RA, **CD4dim, CD19, CD39, CD127dim**	CD314/NKG2D, CCR5, CXCR3, CD159a/NKG2A, CD95/Fas
21	CD8+	CD45RA Terminal Effector (2)	CD3, CD8, CD45RA	CD314/NKG2D, **CCR5, CXCR3, PD1, CD95/Fas**
22	CD8+	CD45RA Terminal Effector (3)	CD3, CD8, CD45RA, **CD16, CD127**	CD314/NKG2D, **CCR5, CXCR3, PD1dim, CD95/Fas**
23	CD8+	CD45RA Terminal Effector (4)	CD3, CD8, CD45RA	CD314/NKG2D, **CCR5**
24	CD8+	CD45RA Terminal Effector (5)	CD3, CD8, CD45RA, **CD57**	CD314/NKG2D
25	CD8+	CD45RA Terminal Effector (6)	CD3, CD8, CD45RA, **CD39dim**	CD314/NKG2D, **CCR5, CXCR3, CD159a/NKG2A**
26	CD8+	CD45RA Terminal Effector (7)	CD3, CD8, CD45RA, **CD127**	CD314/NKG2D, **CCR5, CXCR3, PD1**
27	CD8+	Early like effector (1)	CD3, CD8, CD16dim, CD28, CD141	PD1, CXCR3, CCR5, CD314/NKG2D, CD95/Fas
28	CD8+	Early like effector (2)	CD3, CD8, CD16dim, CD28, CD141	PD1, CXCR3, CCR5, CD314/NKG2D, CD95/Fas, **CD159c/NKG2Cdim, HLA-DR dim**
29	CD8+	Intermediate effector	CD3, CD8, CD25, CD27, CD38, CD127	PD1, CXCR3, CCR5,CD314/NKG2D, CD95/Fas
30	CD8+	Central memory	CD3, CD8, CD28, CD123dim	PD1dim, CD95/Fas, CXCR3, CCR5, CCR7, CD314/NKG2D
31	CD8+	Naïve like	CD3, CD8, CD4dim, CD39, CD45RA	CXCR3, CCR5, CCR7, CD314/NKG2D, CD95/Fas, CD159c/NKG2C
32	CD4+	Early like effector (1)	CD3, CD4, CD28, **CD127**	**CCR5, CD95/Fas**
33	CD4+	Early like effector (2)	CD3, CD4, CD28, **CD127, CD25dim**	**CCR5, CD95/Fas, CXCR3**
34	CD4+	Early like effector (3)	CD3, CD4, CD28, **CD127**	**CD95/Fas**
35	CD4+	Early like effector (4)	CD3, CD4, CD28, **CD127**	**CCR5,CD95/Fas, CXCR3, CD159c/NKG2A, CCR7**
36	CD4+	Early like effector (5)	CD3, CD4, CD28, **CD127, CD141**	**CCR5, CD95/Fas, PD1, CXCR3, CD159c/NKG2C**
37	CD4+	Early like effector (6)	CD3, CD4, CD28, **CD127dim**	**CCR5, CD95/Fas, PD1,CXCR3**
38	CD4+	Early like effector (7)	CD3, CD4, CD28, **CD25, CD39dim**	**CCR5, CD95/Fas, PD1**
39	CD4+	Early like effector (8)	CD3, CD4, CD28, **CD127, CD38 dim, CD39**	**CCR5, CD95/Fas, PD1, CD159c/NKG2C**
40	CD4+	Early like effector (9)	CD3, CD4, CD28, **CD127, CD39**	**CCR5, CD95/Fas, PD1**
41	CD4+	Early effector	CD3, CD4, CD27dim, CD28, CD38	PD1, CD95/Fas
42	CD4+	Central memory (1)	CD3, CD4, CD28, **CD38, CD39, CD19dim, CD27dim, CD16dim**	CCR7, CD95/Fas, **PD1, CCR5, CD159c/NKG2C, CD159a/NKG2Adim**
43	CD4+	Central memory (2)	CD3, CD4, CD28	CCR7, CD95/Fas
44	CD4+	Central memory (3)	CD3, CD4, CD28	CCR7, CD95/Fas, **PD1, CCR5, CXCR3**
45	CD4+	Central memory (4)	CD3, CD4, CD28, **CD127**	CCR7, CD95/Fas, **PD1, CCR5, CXCR3**
46	CD4+	Naïve	CD3, CD4dim, CD27, CD28, CD45RA	CCR7
47	CD4+	Tfh	CD3, CD4, CD27, CD28, CD38	PD1, CXCR3, CCR7, CD95/Fas, CD159c/NKG2C, CD159a/NKG2A dim
48	CD4+	Treg CD45RA-/CD39+	CD3, CD4, CD25, CD27, CD28, CD39	CD95/Fas
49	CD4+	Terminal effector	CD3, CD4	PD1, CXCR3, CCR5
50	CD4+	CD45RA Terminal Effector	CD3, CD4, CD45RA, CD57, CD141dim	
51	CD4+/CD8+ T cells (1)		CD3, CD4, CD8dim, CD28dim, **CD39**	CCR5, PD1, CD95/Fas,
52	CD4+/CD8+ T cells (2)		CD3, CD4, CD8dim, CD28dim, **CD127**	CCR5
53	CD4-/CD8- T cells (1)		CD2, CD3, **CD39**	CCR5, PD1, CCR6
54	CD4-/CD8- T cells (2)		CD2, **CD3dim, CD16dim, CD45RA**	CCR5, CD314/NKG2D
55	CD4-/CD8- T cells (3)		**CD2dim, CD3, CD28, CD127**	
56	CD4-/CD8- T cells (4)		CD2, CD3, **CD27, CD28, CD38**	**PD1, CD95/Fas**
57	NKT like cells	CD2- (1)	CD3, CD8, CD56, CD39dim	CCR5, CD314/NKG2D, **PD1, CXCR3, CD159a/NKG2A, CCR7**
58	NKT like cells	CD2- (2)	CD3, CD8, CD56, CD39, **CD123**	CCR5, CD314/NKG2D, **PD1, CXCR3,**
59	NKT like cells	CD2- (3)	CD3, CD8, CD56, CD39, **CD127dim**	CCR5,CD314/NKG2D, **PD1**
60	NKT like cells	CD2- (4)	CD3, CD8, CD56,CD39	CCR5, CD314/NKG2D, **CXCR3, CD159a/NKG2A**
61	NKT like cells	CD2- (5)	CD3, CD8, CD56	CCR5, CD314/NKG2D, **PD1, CXCR3**
62	NKT like cells	CD2- (6)	CD3, CD8, CD56, CD39, **CD38**	CCR5, CD314/NKG2D, **CXCR3, CD95/Fas, CD159a/NKG2A**
63	NKT like cells	CD2- (7)	CD3, **CD4**, CD56, **CD25dim, CD45RA, CD28, CD127**	CCR5, **PD1dim, CD95/Fas**
64	NKT like cells	CD2+CD8-	CD3, CD56, CD127	PD1, CXCR5, CCR6, CCR7, CD95/Fas
65	Tregs	CD45RA- CD39+ (1)	CD3, CD4, CD2, CD25, CD28, CD39, **CD24, CD141**	CCR7, CD95/Fas, CD159c/NKG2C, HLA-DR, CXCR5, **CCR5, CD11c**
66	Tregs	CD45RA- CD39+ (2)	CD3, CD4, CD2, CD25, CD28, CD39, **CD16**	CCR7, CD95/Fas, CD159c/NKG2C, HLA-DR, CXCR5**dim, PD1**
67	Tregs	CD45RA- CD39- (1)	CD3, CD4, CD27, CD28, CD127, **CD25, CD38,**	PD1, CXCR3, CD95/Fas, CCR7, **CCR5**
68	Tregs	CD45RA- CD39- (2)	CD3, CD4, CD27, CD28, CD127	PD1, CXCR3, CD95/Fas, CCR7**dim**
69	Tregs	CD45RAdim, CD39-	CD3, CD4, CD16, CD25, CD28, CD2	CD95/Fas, CD159c/NKG2C, HLA-DR, **CCR5**
70	Tregs	CD45RAdim, CD39+	CD3, CD4, CD16, CD25, CD28, CD2, **CD39**	CD95/Fas, CD159c/NKG2C, HLA-DR, **CXCR5, CCR6, CD337/NKP30, PD1**
71	Tγδ		CD3, Tγδ, CD2, CD25, CD56dim, CD38dim, CD39dim	CXCR3, CCR5, CCR6, CD159a/NKG2A, CD314/NKG2D
72	Unknown		Tγδdim, CD38dim, CD39dim	
73	B cells	Memory IgM-	CD45RA, CD2, CD24, CD25, CD39	CD11c, HLA-DR, CD1c, CD159c/NKG2C, **CCR6dim**
74	B cells	Memory IgM+	CD45RA, CD2, CD24, CD25, CD39	CD11c, HLA-DR, CD1c, CD159c/NKG2C, **IgM+**
75	B cells	Plasmablasts (1)	CD19, CD27, CD28, CD38, CD39, **CD8, CD141**	CD95/Fas, **CD1c**
76	B cells	Plasmablasts (2)	CD19, CD27, CD38, CD39, **CD127, Tgd**	CD95/Fas, **HLA-DR**
77	B cells	Plasmablasts (3)	CD19, CD27dim, CD38, CD39, **Tgd**	CD95/Fas
78	B cells	Plasmablasts (4)	CD19, CD27dim, CD38, CD39	
79	NK	Early NK (1)	CD27, CD38, CD39, CD56	**CD314/NKG2Ddim**
80	NK	Early NK (2)	CD27, CD38, CD39, CD56, **CD19**	
81	NK	Early NK (3)	CD27, CD38, CD39, CD56, **CD19**	**CD159a/NKG2A**
82	NK	Mature NK	CD16, CD38, CD56, CD45RA	

Table 1. Cell cluster identification. For each for the 82 identified clusters the cell population to which it belongs is shown, together with the specific subset, phenotype and expression of functional markers. Markers highlighted in bold denote differential expression within the same population.

regard, it is also important to highlight that the lack of regional variability was confirmed by both hierarchical and non-supervised approaches.

As for the latter, and as opposed to the classical gating approaches that have identified a total of 52 different immune subsets, the unsupervised clustering revealed a total of 82 subsets. Besides, a total of 19 different subsets have been founds within the Terminal effector CD8+ subset. Although we are aware that obviously not all of
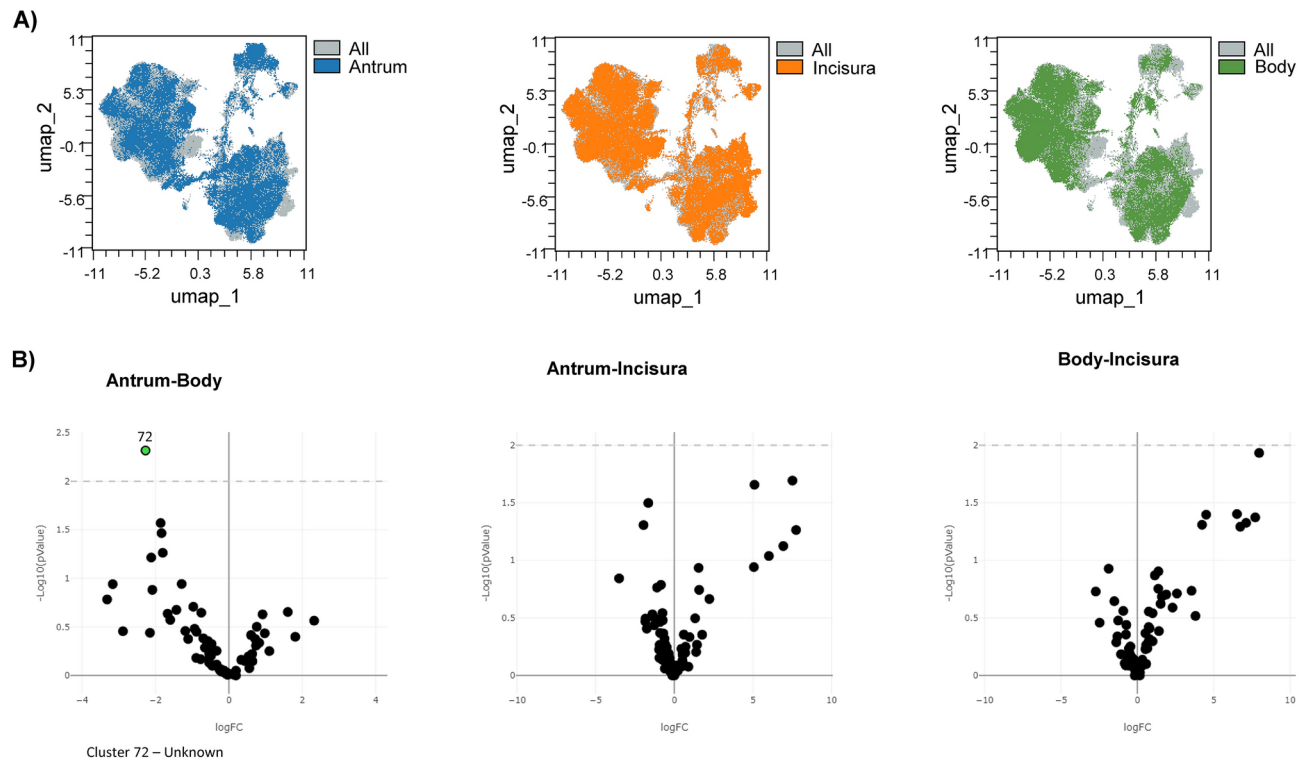
Fig. 5. Regional differences in the immune subset compositions within the human gastric mucosa. (**A**) Within the general UMAP analysis, the relative contribution of the antrum, incisura and body locations were uploaded. (**B**) Volcano plots analyses among the 3 different locations were performed in pairs. A p-value < 0.01 was considered significant and highlighted as green.

them may be biologically relevant but on the contrary resemble different maturation or evolutionary stages, these approaches are valid to identify the great degree of variability that can be found within a given cell population when addressing a new cell type, tissue or condition.

Last, but not least, we are also aware of the limitations of this pilot study, being obviously the main one the restricted sample size which limits for instance the analysis of the different gastritis phenotypes. Besides, and keeping in mind the multistep process of gastric carcinogenesis and the relevance of assessing early precancerous changes, we are also aware that we did not include patients from that type on our analysis. Therefore, future studies should address these issues in larger cohorts and/or perform longitudinal studies to address these changes. However, and although from a clinical point of view taking biopsies from antrum, incisura and body allows the stratification of gastric cancer by differentiating high versus low gastric cancer risk patients when metaplasia is spreading[13], a strength derived from our study is that immune studies can avoid the sampling from the 3 locations given the lack of regional variability.

In summary, we hereby have performed a deep unbiased characterization of the human gastric immune system using top-of-the-art spectral cytometry analysis and subsequent computational cytometry analyses pipeline. These results have therefore a direct clinical implication given that, due to the lack of regional variability within the human gastric mucosa, and the large immune diversity displayed among different individuals, future studies should address this large inter-individual variability by recruiting a large numbers of patients at the time that they can avoid the regional variability hence focusing in the study of one single mucosal location. Our findings remark the importance of personalized medicine and customized treatments based on individual patient characteristics.
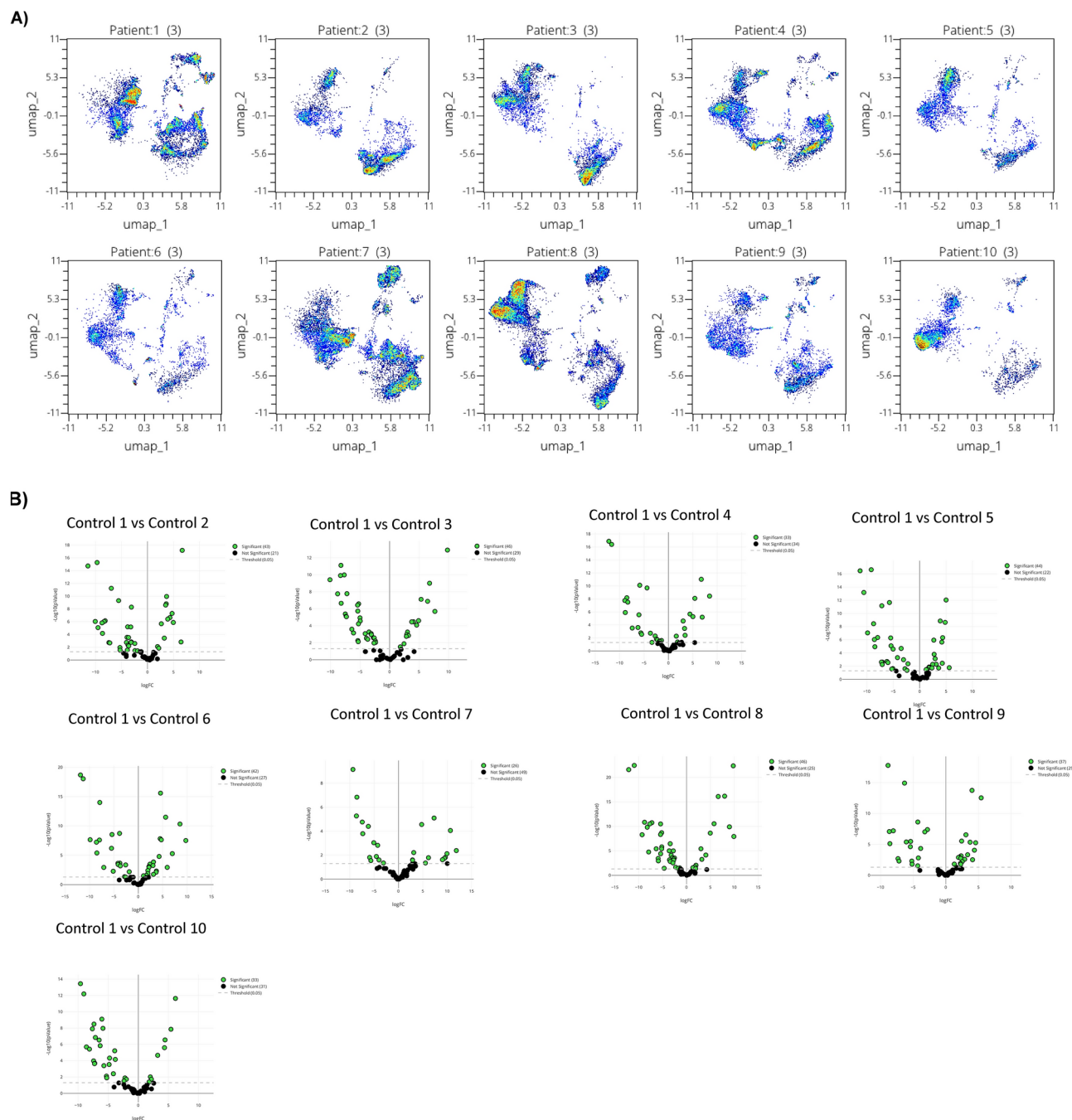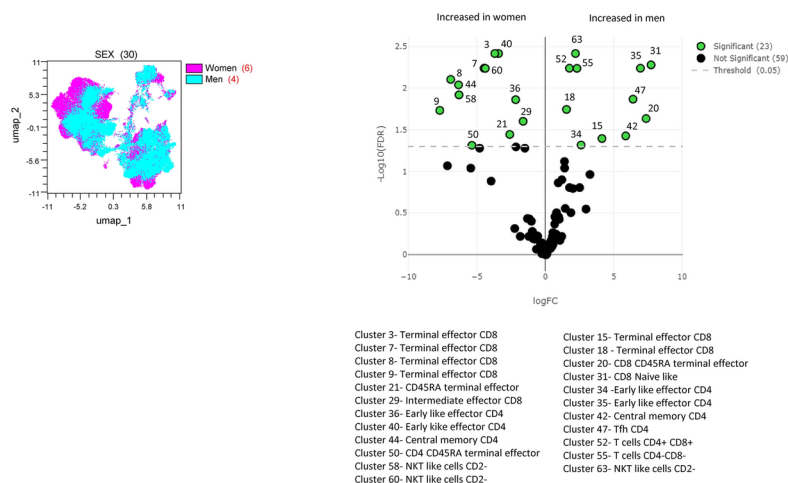
Fig. 6. Individual factors underlaying the immune differences in the human gastric mucosa. (**A**) Within the general UMAP analysis, the relative contribution of the 10 different individuals were uploaded. (**B**) The cellular clusters identified in Fig. 4, were compared from the first control with the other 9 individuals by paired volcano plots analyses. A p-value < 0.05 was considered significant and highlighted as green.
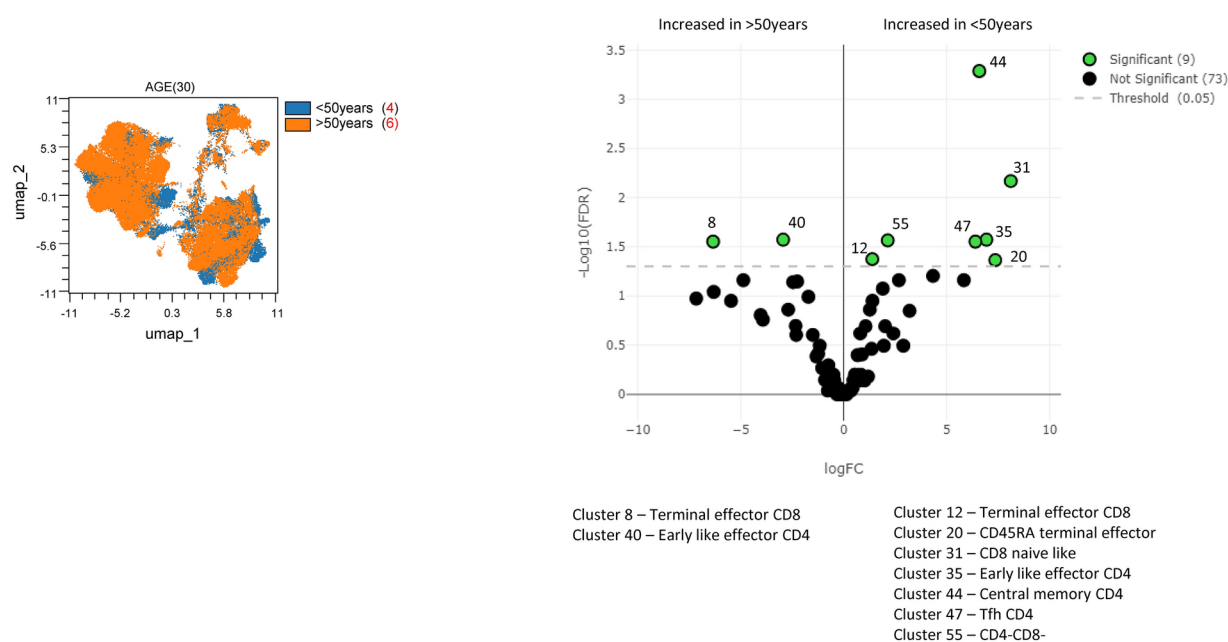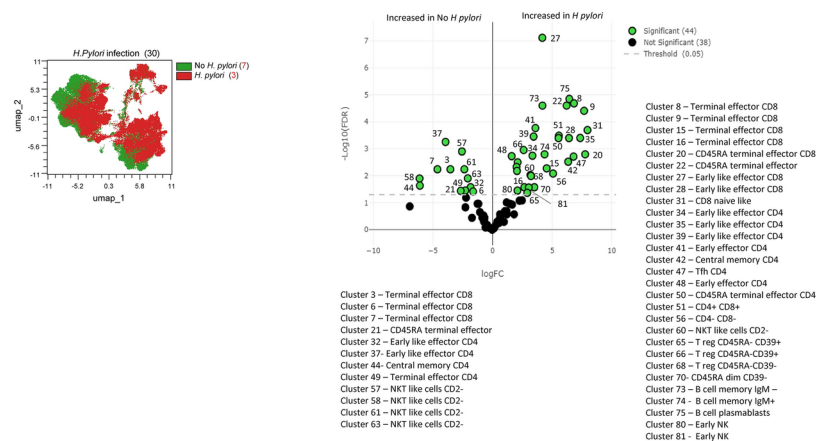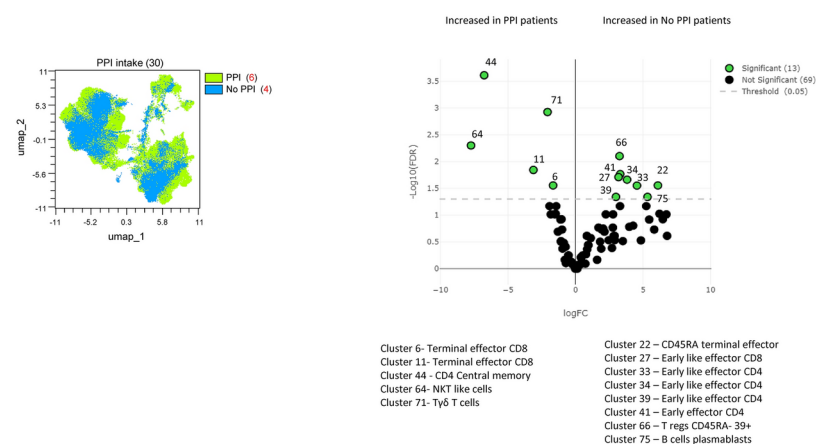
A)

Cluster 3- Terminal effector CD8
Cluster 7- Terminal effector CD8
Cluster 8- Terminal effector CD8
Cluster 9- Terminal effector CD8
Cluster 21- CD45RA terminal effector
Cluster 29- Intermediate effector CD8
Cluster 36- Early like effector CD4
Cluster 40- Early kike effector CD4
Cluster 44- Central memory CD4
Cluster 50- CD4 CD45RA terminal effector
Cluster 58- NKT like cells CD2-
Cluster 60- NKT like cells CD2-

Cluster 15- Terminal effector CD8
Cluster 18 - Terminal effector CD8
Cluster 20- CD8 CD45RA terminal effector
Cluster 31- CD8 Naive like
Cluster 34 -Early like effector CD4
Cluster 35- Early like effector CD4
Cluster 42- Central memory CD4
Cluster 47- Tfh CD4
Cluster 52- T cells CD4+ CD8+
Cluster 55- T cells CD4-CD8-
Cluster 63- NKT like cells CD2-

B)

Cluster 8 – Terminal effector CD8
Cluster 40 – Early like effector CD4

Cluster 12 – Terminal effector CD8
Cluster 20 – CD45RA terminal effector
Cluster 31 – CD8 naive like
Cluster 35 – Early like effector CD4
Cluster 44 – Central memory CD4
Cluster 47 – Tfh CD4
Cluster 55 – CD4-CD8-

Fig. 7. Immune differences among the different study cohorts Metadata differences in the immune subset compositions within the human gastric mucosa. UMAP analysis and volcano plots were applied to identify, within all the studied samples, the presence of clusters differentially represented in the human gastric mucosa based on the (**A**) sex, (**B**) patients having proton pump inhibitor (PPI) intake, (**C**) *Helicobacter pylori* infection, (**D**) age and (**E**) presence/absence of dyspepsia (**E**).
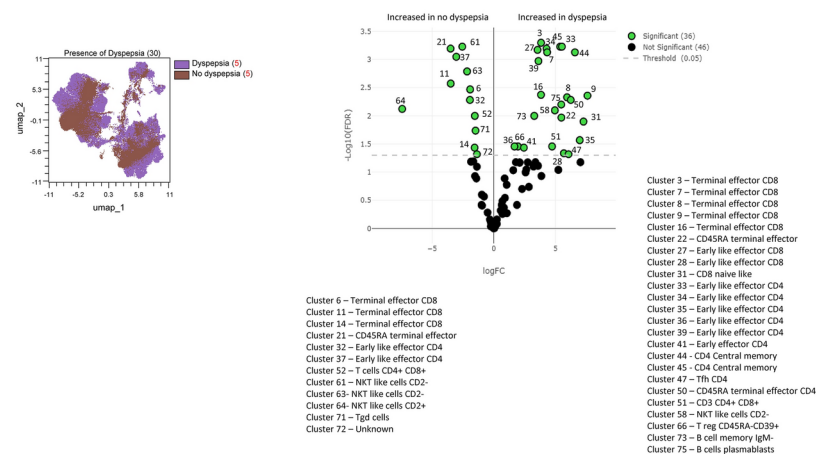
Figure 7. (continued)

	SEX		AGE		IBP intake		HP infection		Symptoms	
	Men	Women	Over 50	Under 50	Yes	No	Yes	No	Dyspepsia	No dyspepsia
Cluster 3- Terminal effector CD8	↓	↑	n/a	n/a	n/a	n/a	↓	↑	↑	↓
Cluster 6- Terminal effector CD8	n/a	n/a	n/a	n/a	↑	↓	↓	↑	↓	↑
Cluster 7- Terminal effector CD8	↓	↑	n/a	n/a	n/a	n/a	↓	↑	↑	↓
Cluster 8- Terminal effector CD8	↓	↑	↑	↓	n/a	n/a	↑	↓	↑	↓
Cluster 9- Terminal effector CD8	↓	↑	n/a	n/a	n/a	n/a	↑	↓	↑	↓
Cluster 11- Terminal effector CD8	n/a	n/a	n/a	n/a	↑	↓	n/a	n/a	↓	↑
Cluster 15- Terminal effector CD8	↑	↓	n/a	n/a	n/a	n/a	↑	↓	n/a	n/a
Cluster 16 – Terminal effector CD8	n/a	n/a	n/a	n/a	n/a	n/a	↑	↓	↑	↓
Cluster 20- CD8 CD45RA terminal effector	↑	↓	↓	↑	n/a	n/a	↑	↓	n/a	n/a
Cluster 21- CD45RA terminal effector	↓	↑	n/a	n/a	n/a	n/a	↑	↓	↓	↑
Cluster 22 – CD45RA terminal effector	n/a	n/a	n/a	n/a	↓	↑	↑	↓	↑	↓
Cluster 27 – Early like effector CD8	n/a	n/a	n/a	n/a	↓	↑	↑	↓	↑	↓
Cluster 28 – Early like effector CD8	n/a	n/a	n/a	n/a	n/a	n/a	↑	↓	↑	↓
Cluster 31- CD8 Naïve like	↑	↓	↓	↑	n/a	n/a	↑	↓	↑	↓
Cluster 32- Early like effector CD4	n/a	n/a	n/a	n/a	n/a	n/a	↓	↑	↓	↑
Cluster 33 – Early like effector CD4	n/a	n/a	n/a	n/a	↓	↑	n/a	n/a	↑	↓
Cluster 34 - Early like effector CD4	↑	↓	n/a	n/a	↓	↑	↑	↓	↑	↓
Cluster 35- Early like effector CD4	↑	↓	↓	↑	n/a	n/a	↑	↓	↑	↓
Cluster 36- Early like effector CD4	↓	↑	n/a	n/a	n/a	n/a	n/a	n/a	↑	↓
Cluster 37- Early like effector CD4	n/a	n/a	n/a	n/a	n/a	n/a	↓	↑	↓	↑
Cluster 39 – Early like effector CD4	n/a	n/a	n/a	n/a	↓	↑	↑	↓	↑	↓
Cluster 40- Early kike effector CD4	↓	↑	↑	↓	n/a	n/a	n/a	n/a	n/a	n/a
Cluster 41 – Early effector CD4	n/a	n/a	n/a	n/a	↓	↑	↑	↓	↑	↓
Cluster 42- Central memory CD4	↑	↓	n/a	n/a	n/a	n/a	↑	↓	n/a	n/a
Cluster 44- Central memory CD4	↓	↑	↓	↑	↑	↓	↓	↑	↑	↓
Cluster 47- Tfh CD4	↑	↓	↓	↑	n/a	n/a	↑	↓	↑	↓
Cluster 50- CD4 CD45RA terminal effector	↓	↑	n/a	n/a	n/a	n/a	↑	↓	↑	↓
Cluster 51 – CD4+ CD8+	n/a	n/a	n/a	n/a	n/a	n/a	↑	↓	↑	↓
Cluster 52- T cells CD4+ CD8+	↑	↓	n/a	n/a	n/a	n/a	n/a	n/a	↓	↑
Cluster 55- T cells CD4-CD8-	↑	↓	↓	↑	n/a	n/a	n/a	n/a	n/a	n/a
Cluster 58- NKT like cells CD2-	↓	↑	n/a	n/a	n/a	n/a	↓	↑	↑	↓
Cluster 60- NKT like cells CD2-	↓	↑	n/a	n/a	n/a	n/a	↑	↓	n/a	n/a
Cluster 61 – NKT like cells CD2-	n/a	n/a	n/a	n/a	n/a	n/a	↓	↑	↓	↑
Cluster 63- NKT like cells CD2-	↑	↓	n/a	n/a	n/a	n/a	↓	↑	↓	↑
Cluster 66 – T regs CD45RA- CD39+	n/a	n/a	n/a	n/a	↓	↑	↑	↓	↑	↓
Cluster 71- Tgd T cells	n/a	n/a	n/a	n/a	↑	↓	n/a	n/a	↓	↑
Cluster 73 – B cell memory IgM –	n/a	n/a	n/a	n/a	n/a	n/a	↑	↓	↑	↓
Cluster 75 – B cells plasmablasts	n/a	n/a	n/a	n/a	↓	↑	↑	↓	↑	↓

Table 2. Cluster differences among cohorts. Results from Fig. 7 are summarized displaying, for each cell cluster that is statistically significant among the cohort comparison, where it was increased (↑) or decreased (↓) in each cohort.
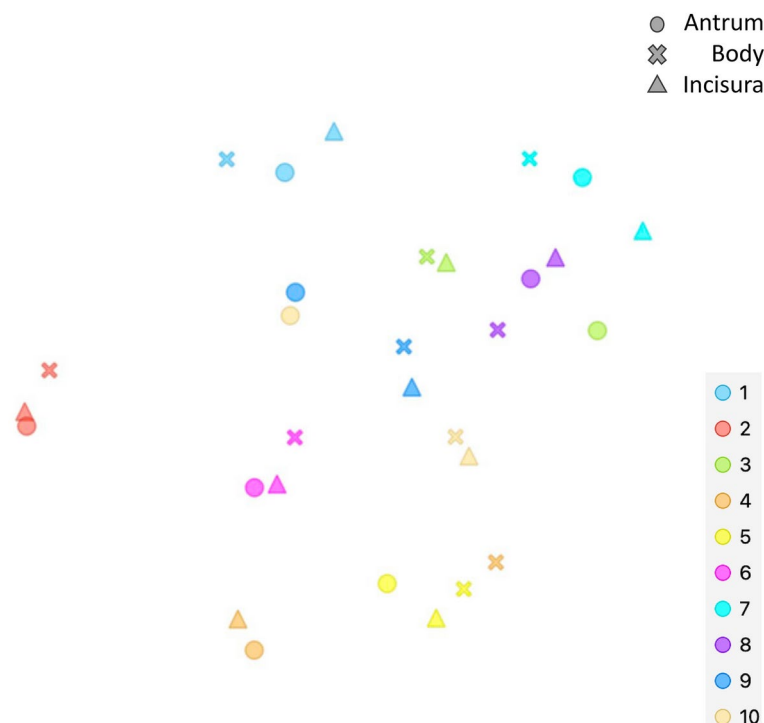
Fig. 8. tSNE analysis confirmed interindividual variability and lack of regional variation in the human gastric mucosa. A tSNE analysis was performed, based on the relative proportion of each of the 52 different immune cell subsets identified in Fig. 1 and, within each of them, the median fluorescence index (MFI) for the expression of NKG2a, NKG2c, NKG2d, NKP30, CCR5, CCR6, CXCR3, CXCR5, FAS, PD-1 and CD57. Samples from each individual are identified by a colour code, while the sample location is identified by a symbol (Black circle : antrum; Black triangle : incisura : body).

Data availability

The datasets used and/or analyzed during the current study available from the corresponding author on reasonable request.

References

1. Spitzer, M. H. & Nolan, G. P. Mass cytometry: Single cells many features. *Cell* **165**, 780–791 (2016).
2. Bendall, S. C., Nolan, G. P., Roederer, M. & Chattopadhyay, P. K. A deep profiler's guide to cytometry. *Trends Immunol.* **33**, 323–332 (2012).
3. Nair, N. et al. Mass cytometry as a platform for the discovery of cellular biomarkers to guide effective rheumatic disease therapy. *Arthritis Res. Ther.* **17**, 127 (2015).
4. Gaudillière, B. et al. Clinical recovery from surgery correlates with single-cell immune signatures. *Sci. Transl. Med.* **6**, 255 (2014).
5. Fergusson, J. R. et al. CD161 defines a transcriptional and functional phenotype across distinct human T cell lineages. *Cell Rep.* **9**, 1075–1088 (2014).
6. de Vries, N. L. et al. High-dimensional cytometric analysis of colorectal cancer reveals novel mediators of antitumour immunity. *Gut* **69**, 691–703 (2020).
7. Shinko, D. et al. Mass cytometry reveals a sustained reduction in CD16+ natural killer cells following chemotherapy in colorectal cancer patients. *Front. Immunol.* https://doi.org/10.3389/fimmu.2019.02584 (2019).
8. van Unen, V. et al. Mass cytometry of the human mucosal immune system identifies tissue- and disease-associated immune subsets. *Immunity* **44**, 1227–1239 (2016).
9. Tyler, C. J. et al. Implementation of mass cytometry as a tool for mechanism of action studies in inflammatory bowel disease. *Inflamm. Bowel Dis.* **24**, 2366–2376 (2018).
10. Kinchen, J. et al. Structural remodeling of the human colonic mesenchyme in inflammatory bowel disease. *Cell* **175**, 372-386.e17 (2018).
11. Mitsialis, V. et al. Single-cell analyses of colon and blood reveal distinct immune cell signatures of ulcerative colitis and crohn's disease. *Gastroenterology* **159**, 591-608.e10 (2020).
12. Correa, P. A human model of gastric carcinogenesis. *Cancer Res.* **48**, 3554–3560 (1988).
13. Banks, M. et al. British society of gastroenterology guidelines on the diagnosis and management of patients at risk of gastric adenocarcinoma. *gut* **68**, 1545–1575 (2019).
14. Mowat, A. M. & Agace, W. W. Regional specialization within the intestinal immune system. *Nat. Rev. Immunol.* **14**, 667–685 (2014).
15. Agace, W. W. & McCoy, K. D. Regionalized development and maintenance of the intestinal adaptive immune landscape. *Immunity* **46**, 532–548 (2017).

16. Bernardo, D. et al. Chemokine (C-C Motif) receptor 2 mediates dendritic cell recruitment to the human colon but is not responsible for differences observed in dendritic cell subsets, phenotype, and function between the proximal and distal colon. *Cell. Mol. Gastroenterol. Hepatol.* **2**, 22-39.e5 (2016).

17. Park, L. M., Lannigan, J. & Jaimes, M. C. <scp>OMIP-069</scp>: Forty-color full spectrum flow cytometry panel for deep immunophenotyping of major cell subsets in human peripheral blood. *Cytom. Part A* **97**, 1044–1051 (2020).

18. Ugalde-Triviño, L. et al. Circulating immunome fingerprint in eosinophilic esophagitis is associated with clinical response to proton pump inhibitor treatment. *Front. Immunol.* https://doi.org/10.3389/fimmu.2024.1374611 (2024).

19. H-Vazquez, J., Cal-Sabater, P., Arribas-Rodríguez, E., Fiz-López, A., Perez-Segurado, C., Martín-Muñoz, Á., & De Prado, Á., Unbiased spectral cytometry immunome characterization predicts COVID-19 mRNA vaccine failure in older adults and patients with lymphoid malignancies. *medRxiv* (2013).

20. Bernardo, D. et al. Human intestinal pro-inflammatory CD11chighCCR2+CX3CR1+ macrophages, but not their tolerogenic CD11c−CCR2−CX3CR1− counterparts, are expanded in inflammatory bowel disease. *Mucosal Immunol.* **11**, 1114–1126 (2018).

21. G. de Castro, C., G. del Hierro, A., H-Vázquez, J., Cuesta-Sancho, S. & Bernardo, D. State-of-the-art cytometry in the search of novel biomarkers in digestive cancers. *Front. Oncol.* **1**, (2024).

22. Bagheri, N. et al. Downregulated regulatory T cell function is associated with increased peptic ulcer in Helicobacter pylori-infection. *Microb. Pathog.* **110**, 165–175 (2017).

23. Wu, Y.-Y. et al. Recruitment of CCR6+ Foxp3+ regulatory gastric infiltrating lymphocytes in Helicobacter pylori gastritis. *Helicobacter* **24**, e12550 (2019).

24. Talayev, V. et al. CCR6+ T helper cells and regulatory T cells in the blood and gastric mucosa during Helicobacter pylori infection. *Helicobacter* **29**, e13097 (2024).

25. Bornschein, W. Clinical studies using a photometric method for determining serum lipase activity. *Leber. Magen. Darm* **14**, 125–128 (1984).

26. Majewski, M. et al. Microbiota and the immune system-actors in the gastric cancer story. *Cancers (Basel).* **14**, 3832 (2022).

27. Groen-van Schooten, T. S. et al. Phenotypic immune characterization of gastric and esophageal adenocarcinomas reveals profound immune suppression in esophageal tumor locations. *Front. Immunol.* **15**, 1372272 (2024).

Acknowledgements

Author contributions

SI, DC and LFS performed patient recruitment and obtained the biological samples and the clinical data. Sample processing and experimental approaches were performed by AdP, PCS, AFL, EAR, AMM, CP, JAG and EA. Computational cytometry approaches were performed by FPC, JH, CM and SCS. Study was designed by LFS who coordinated and supervised the study together with DB (who also obtained the funds to perform the study). Manuscript was drafted by AdP and SCS, and further edited by CM, JAG, EA and DB. All authors reviewed and approved the final version of the manuscript.

Funding

Declarations

Competing interests

The authors declare no competing interests.

Additional information

Supplementary Information The online version contains supplementary material available at https://doi.org/10.1038/s41598-024-78908-z.

Correspondence and requests for materials should be addressed to D.B.

Reprints and permissions information is available at www.nature.com/reprints.

Publisher's note Springer Nature remains neutral with regard to jurisdictional claims in published maps and institutional affiliations.